# Space charge modeling method in 2.5D for scaling fixed-field alternating-gradient accelerators

Kai Zhou,[1,2] Ming-Yang Huang,[1,2,3,*] Xiao Li,[1,2,3,†] Bin Wu,[1,2] Hanyang Liu,[1,2] Shouyan Xu,[1,2] and Sheng Wang[1,2,3]

[1]*Institute of High Energy Physics, Chinese Academy of Sciences, Beijing 100049, China*
[2]*Spallation Neutron Source Science Center, Dongguan 523803, China*
[3]*University of Chinese Academy of Sciences, Beijing 100049, China*

(Received 10 June 2026; accepted 23 October 2026; published 5 November 2026)

Scaling fixed-field alternating-gradient accelerators (scaling FFAs) are promising candidates for high-intensity proton drivers, for which space charge effects are a key limitation of beam performance. For long bunches in circular accelerators, 2.5D space charge methods provide an efficient alternative to full 3D PIC methods by exploiting the large longitudinal-to-transverse aspect ratio of the bunch. In scaling FFAs, however, the reference closed orbit varies with particle energy, and the transverse and longitudinal directions are not directly available in cylindrical coordinates. Therefore, the longitudinal slicing and transverse planes required by a 2.5D model must be reconstructed dynamically, rather than defined from a single fixed reference orbit, which poses a central challenge for efficient 2.5D modeling in high-intensity scaling FFAs. This paper presents a new 2.5D space charge modeling method for high-intensity scaling FFAs and its implementation in the PyFFA code. The central idea is to replace the fixed reference orbit used in conventional 2.5D models with a dynamically reconstructed local reference frame based on a precomputed family of energy-dependent closed orbits. During tracking, this frame is updated according to the instantaneous particle state, enabling transverse Poisson equations to be solved consistently in this dynamic local coordinate system. The resulting space charge field is then transformed back to global cylindrical coordinates and applied in the tracking equations. Benchmarks of space charge fields, tune shifts, rms envelope evolution, and longitudinal phase-space evolution show good agreement with analytical results, validating the field calculation and its coupling to beam dynamics for long, arc-shaped bunches in scaling FFAs. The implemented model enables efficient studies of space charge effects on beam dynamics in high-intensity scaling FFAs.

DOI: 10.1103/q1xb-z29j

## I. INTRODUCTION

High-intensity proton accelerators are key driver platforms for spallation neutron sources, muon sources, and advanced isotope production facilities [1–5]. These facilities are typically operated in a pulsed mode, in which a large number of particles are accumulated within a single pulse through multiturn injection, leading to high peak beam intensity. Space charge effects are among the key factors that limit beam quality and intensity in such machines. Therefore, establishing a suitable numerical model for space charge is a fundamental requirement for high-intensity beam dynamics studies.

The choice of a space charge model is closely related to the bunch geometry. For bunches with comparable transverse and longitudinal dimensions, 3D particle-in-cell (PIC) methods provide a general description of self-fields for complex charge distributions. However, for long bunches in circular accelerators, where the longitudinal bunch size is much larger than the transverse size, a full 3D PIC calculation on a Cartesian mesh remains general but may require a large computational domain to cover the full bunch length while resolving the much smaller transverse dimensions. In this regime, much of the Cartesian mesh may remain unoccupied by particles, reducing mesh efficiency and increasing the computational cost. Such an approach can therefore become computationally demanding, and in some cases even impractical, for routine high-intensity tracking studies. This geometrical mismatch between a Cartesian PIC mesh and a long, arc-shaped bunch is illustrated in Fig. 1. A commonly used alternative is a 2.5D space charge model [6,7], in which the bunch is divided into a sequence of longitudinal slices and a 2D

*Contact author: huangmy@ihep.ac.cn
†Contact author: lixiao@ihep.ac.cn

*Published by the American Physical Society under the terms of the Creative Commons Attribution 4.0 International license. Further distribution of this work must maintain attribution to the author(s) and the published article's title, journal citation, and DOI.*

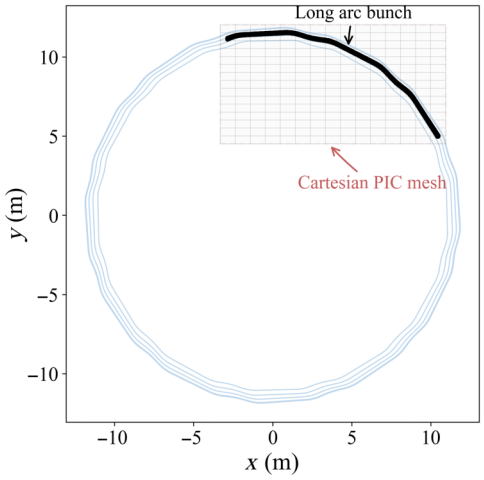



FIG. 1. Schematic illustration of the geometrical mismatch between a Cartesian PIC mesh and a long, arc-shaped bunch in a circular accelerator. For such a bunch geometry, a Cartesian-grid 3D PIC calculation may require a large mesh domain while only a small fraction of the mesh overlaps with the beam distribution, reducing mesh efficiency.

Poisson problem is solved on the transverse plane of each slice. This slice-based formulation exploits the large longitudinal-to-transverse aspect ratio of the bunch and reduces the computational cost while retaining the dominant transverse self-field; longitudinal self-field effects can be included through an additional line-charge treatment when needed.

Spiral-sector scaling fixed-field alternating-gradient accelerators (spiral scaling FFAs) combine fixed magnetic fields, strong focusing, and large momentum acceptance, and are considered promising candidates for high-power proton drivers [8–11]. Space charge modeling in scaling FFAs, however, remains challenging. Although the bunch in a high-intensity scaling FFA can still be regarded as a long bunch, its geometry is more complicated than that in rings with a fixed reference orbit. The bunch forms a long arc-shaped distribution along the curved closed orbits, and the closed orbits vary with particle energy. As a result, no single fixed closed orbit can serve as a global reference throughout acceleration. Conventional 2.5D space charge methods based on a fixed reference orbit and its associated local coordinate system therefore cannot be applied directly. In other words, the difficulty of space charge modeling in scaling FFAs is twofold: a Cartesian-grid 3D PIC method is not well matched to the long, arc-shaped bunch geometry and can be computationally inefficient, whereas a conventional 2.5D model relies on a fixed reference orbit and a predefined local coordinate system that are no longer valid.

In recent years, several numerical tools have been developed for high-intensity beam dynamics in scaling FFAs, including Zgoubi [12], OPAL [13], and SCODE [14].

In Zgoubi, space charge has been incorporated through slice-based treatments, where field maps or analytical elements are divided into thin slices and transverse space charge kicks are applied between successive slices. The original studies reported applications mainly based on KV-type beam distributions and slice-based space charge approximations, and explicitly identified more general PIC simulations as necessary for high-intensity beams with nonuniform distributions, emittance growth, and self-consistent collective dynamics [15,16].

OPAL has also been applied to FFA-related beam dynamics studies, but the reported applications have mainly focused on single-particle dynamics rather than high-intensity space charge effects. Although OPAL includes a general 3D PIC space charge solver and has reported applications in isochronous cyclotrons and other short-bunch space charge studies [17], its application to long bunches in high-intensity scaling FFAs has not, to our knowledge, been systematically reported.

SCODE has also incorporated space charge modeling for FFAs, using approaches such as multipole expansions. Nevertheless, recent related work has further emphasized that, for long bunches distributed along curved orbits, the proper definition of a local coordinate system remains one of the key difficulties in space charge modeling [18].

These developments indicate that, although space charge effects in FFAs have been studied to some extent, a clear and systematic modeling framework is still lacking for the scaling FFAs case in which long bunches and nonfixed closed orbits coexist. This has limited, to some degree, further studies of space charge effects in high-intensity scaling FFAs.

Motivated by these considerations, we develop a new 2.5D space charge modeling method for scaling FFAs with long arc-shaped bunches and energy-dependent closed orbits, and implement it in PyFFA [19], a beam dynamics code that we developed for high-intensity scaling FFA simulations. The central idea is to replace the single fixed reference orbit assumed in conventional 2.5D models with a dynamically reconstructed local reference frame based on an energy-dependent closed-orbit family. During tracking, the reference closed-orbit geometry and the corresponding transverse and longitudinal coordinates are reconstructed according to the instantaneous bunch state, allowing the long arc-shaped bunch to be sliced and treated in a local coordinate system consistent with the global cylindrical tracking variables. The transverse space charge field is obtained from slice-by-slice 2D Poisson solves, the longitudinal field is approximated from the line charge density, and the resulting local field components are projected back to the global cylindrical coordinates for particle tracking. The method is validated through benchmarks of transverse and longitudinal electric fields, space charge tune shifts, rms envelope evolution, and

longitudinal phase-space evolution, and is further applied to high-intensity beam dynamics studies related to the CSNS/FFA project.

## II. DIFFICULTIES IN SPACE CHARGE MODELING FOR SCALING FFAS

### A. Numerical tracking framework for FFAs

In scaling FFA beam simulations, particles are usually tracked using field maps in a global cylindrical coordinate system. In this framework, particle trajectories are advanced directly in the global coordinates according to the electromagnetic field distribution, without requiring a single fixed reference orbit for the tracking itself. The motion of a charged particle is governed by the Lorentz force equation

$$\frac{d\mathbf{p}}{dt} = q(\mathbf{E} + \mathbf{v} \times \mathbf{B}), \tag{1}$$

where $\mathbf{p}$ is the particle momentum, $\mathbf{v}$ is the particle velocity, and $q$ is the particle charge. The electromagnetic fields acting on the particle can be decomposed into externally applied fields and beam self-fields:

$$\mathbf{E} = \mathbf{E}_{\text{ext}} + \mathbf{E}_{\text{sc}}, \tag{2}$$

$$\mathbf{B} = \mathbf{B}_{\text{ext}} + \mathbf{B}_{\text{sc}}. \tag{3}$$

Here, $\mathbf{E}_{\text{ext}}$ mainly denotes the external rf accelerating field, and $\mathbf{B}_{\text{ext}}$ denotes the prescribed main magnetic field. The terms $\mathbf{E}_{\text{sc}}$ and $\mathbf{B}_{\text{sc}}$ denote the space charge self-fields.

For a scaling FFA, the vertical magnetic field on the median plane usually has a radial scaling law and an azimuthal flutter structure. It can be written as

$$B_z(r, \theta, 0) = B_{\text{ref}} \left( \frac{r}{r_{\text{ref}}} \right)^k F[\theta - \theta_{\text{sp}}(r)], \tag{4}$$

where $B_{\text{ref}}(r/r_{\text{ref}})^k$ gives the radial scaling of the field amplitude, $B_{\text{ref}}$ is the magnetic field strength at the reference radius $r_{\text{ref}}$, and $k$ is the field index. The function $F$ describes the azimuthal flutter of the magnetic field, and $\theta_{\text{sp}}(r)$ denotes the spiral. In numerical tracking, the external magnetic field can be generated either from the above analytical scaling field model or directly from 2D or 3D field maps.

When the 2D median-plane magnetic field is known, it can be extrapolated to the off-median-plane region from Maxwell's equations under the condition of median-plane symmetry [20]. Defining the transverse Laplacian on the median plane as

$$\nabla^2_{r,\theta} \equiv \frac{\partial^2}{\partial r^2} + \frac{1}{r}\frac{\partial}{\partial r} + \frac{1}{r^2}\frac{\partial^2}{\partial \theta^2}, \tag{5}$$

off-median-plane magnetic field components can be expressed as series expansions in the vertical coordinate $z$:

$$B_r(r, \theta, z) = \sum_{n=0}^{\infty} (-1)^n \frac{z^{2n+1}}{(2n+1)!} \frac{\partial}{\partial r} \left[ (\nabla^2_{r,\theta})^n B_z(r, \theta, 0) \right], \tag{6}$$

$$B_\theta(r, \theta, z) = \frac{1}{r} \sum_{n=0}^{\infty} (-1)^n \frac{z^{2n+1}}{(2n+1)!} \frac{\partial}{\partial \theta} \left[ (\nabla^2_{r,\theta})^n B_z(r, \theta, 0) \right], \tag{7}$$

$$B_z(r, \theta, z) = \sum_{n=0}^{\infty} (-1)^n \frac{z^{2n}}{(2n)!} (\nabla^2_{r,\theta})^n B_z(r, \theta, 0). \tag{8}$$

This expansion provides a commonly used way to construct a near-median-plane 3D magnetic field from a median-plane field map. It also illustrates an important feature of FFA tracking: particles can be advanced directly in the actual magnetic field distribution using global cylindrical coordinates, without relying on a single fixed closed orbit as the global reference trajectory. This differs from the reference-orbit-based formulation commonly used in conventional synchrotron tracking, where transverse and longitudinal coordinates are defined with respect to a prescribed design orbit. In an FFA tracking framework based on global cylindrical variables, the local transverse and longitudinal coordinates required by a 2.5D space charge model are not directly available and must therefore be reconstructed.

Based on this general tracking framework, the PyFFA beam dynamics simulation code has been developed in this work. PyFFA describes particle states in the global cylindrical coordinate system $(r, \theta, z)$ and uses time $t$ as the independent variable. At each integration step, the external rf field, the magnetic field map, and the space charge self-field are evaluated at the particle position and used to integrate the Lorentz equation with a Runge-Kutta method.

### B. Difficulties of applying the 2.5D space charge method to scaling FFAs

As discussed in the Introduction, the long, arc-shaped bunch geometry motivates the use of a slice-based 2.5D treatment. Conventional 2.5D space charge models rely on a local coordinate frame in which the transverse and longitudinal directions are explicitly separated. This frame is usually attached to a fixed reference orbit. In reference-orbit-based synchrotron tracking, particle coordinates are already defined with respect to this orbit, so the 2.5D field calculation and particle tracking can be carried out in the same coordinate system without additional coordinate reconstruction.

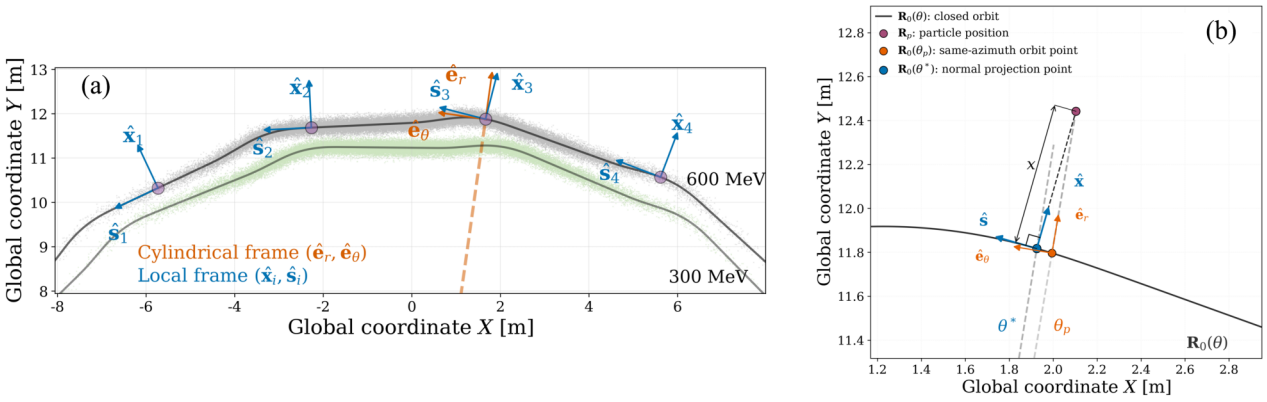



FIG. 2. Coordinate systems and local reference-point construction used in the 2.5D model. (a) Energy-dependent closed orbits and arc-shaped bunches, with the global cylindrical basis $(\hat{\mathbf{e}}_r, \hat{\mathbf{e}}_\theta)$ and local bases $(\hat{\mathbf{x}}_i, \hat{\mathbf{s}}_i)$ reconstructed along the reference orbit. (b) Construction of the local reference point for a particle in the median plane. The same-azimuth point $\mathbf{R}_0(\theta_p)$ gives a radial-type displacement, whereas the normal projection point $\mathbf{R}_0(\theta^*)$ defines the local transverse coordinate $x$.

This situation is fundamentally different in a scaling FFA. During acceleration, the closed orbit changes with particle energy, so no single closed orbit can serve as a fixed reference throughout the process. Longitudinal space charge can further produce energy differences along the bunch, so different longitudinal slices may be associated with different energy-dependent closed orbits. Since PyFFA tracks particles in global cylindrical coordinates rather than in a local orbit-attached frame, the transverse and longitudinal coordinates required by the 2.5D solver are not directly available. They must therefore be reconstructed from the energy-dependent closed-orbit family using the instantaneous particle state.

Figure 2(a) illustrates the energy-dependent closed-orbit family and the relation between the global cylindrical basis and the local transverse-longitudinal basis reconstructed along the orbit.

The longitudinal coordinate also requires special treatment. In cylindrical tracking, the azimuthal coordinate is periodic and therefore cannot directly represent the continuous longitudinal position of a long bunch. In multiturn injection, particles whose azimuthal coordinates differ by an integer multiple of $2\pi$ may still be neighboring particles within the same bunch. Reducing the azimuthal angle modulo $2\pi$ removes the multiturn offset but can artificially split a physically continuous bunch near the 0° boundary, placing neighboring particles on opposite sides of the periodic interval. Therefore, before applying 2.5D slicing, the periodic azimuthal coordinates must be unfolded into a continuous arc-length coordinate that represents the actual longitudinal interval occupied by the bunch.

Finally, the space charge field obtained in the local slice coordinates must be mapped back to the global cylindrical coordinates used for tracking. This back-projection, based on the geometrical relation between the local and global bases, ensures that the self-field components are applied consistently in the Lorentz-force integration.

The main difficulties of 2.5D space charge modeling in a scaling FFA can therefore be summarized as follows. First, the local reference frame and the corresponding bunch coordinates must be reconstructed from the energy-dependent closed orbit family and the instantaneous particle state. Second, the periodicity of the azimuthal coordinate must be removed to recover the continuous longitudinal interval occupied by the bunch, especially in multiturn injection. Third, the local space charge field must be consistently transformed back to the global cylindrical coordinates used for particle tracking. The following sections address these issues through reconstruction of the local transverse coordinates, construction of the continuous longitudinal coordinate, and back-projection of the local field.

## III. RECONSTRUCTION OF LOCAL TRANSVERSE COORDINATES

### A. Reference closed orbit and definition of the local coordinate system

Closed orbits are first computed at a set of discrete kinetic energies and stored on a two-dimensional grid in $E_k$ and $\theta$, where $E_k$ denotes the kinetic energy and $\theta$ is the azimuthal angle. The resulting closed orbit family is represented by the radius function

$$r_0 = r_0(\theta, E_k). \tag{9}$$

During tracking, a common closed orbit interpolated at the instantaneous mean kinetic energy of the bunch is first used for the longitudinal mapping and slice assignment.

Several geometrical quantities are precomputed from this closed orbit family for local coordinate reconstruction. For each closed orbit, the azimuthal derivative of the radius is computed as

$$r_0'(\theta, E_k) = \frac{\partial r_0(\theta, E_k)}{\partial \theta}. \tag{10}$$

The corresponding arc-length metric factor is then given by

$$h(\theta, E_k) = \sqrt{r_0^2(\theta, E_k) + [r_0'(\theta, E_k)]^2}, \tag{11}$$

so that the differential arc length satisfies

$$ds = h(\theta, E_k) d\theta. \tag{12}$$

The cumulative arc-length coordinate along the closed orbit is obtained as

$$s_0(\theta, E_k) = \int_0^\theta h(\vartheta, E_k) d\vartheta. \tag{13}$$

Consequently, the quantities required for coordinate reconstruction, namely $r_0$, $r_0'$, $h$, and $s_0$, are stored on the same two-dimensional grid in $E_k$ and $\theta$. During tracking, their values at the required energy and azimuthal position are obtained by interpolation.

At a given point on the reference closed orbit, the orbit position in the median plane can be written as

$$\mathbf{R}_0(\theta, E_k) = r_0(\theta, E_k)\mathbf{e}_r(\theta), \tag{14}$$

where $\mathbf{e}_r$ is the radial unit vector of the global cylindrical coordinate system. Differentiating $\mathbf{R}_0$ with respect to $\theta$ gives the tangent direction,

$$\frac{\partial \mathbf{R}_0}{\partial \theta} = r_0'(\theta, E_k)\mathbf{e}_r + r_0(\theta, E_k)\mathbf{e}_\theta. \tag{15}$$

Thus, the local tangential unit vector is

$$\mathbf{e}_s = \frac{r_0'(\theta, E_k)\mathbf{e}_r + r_0(\theta, E_k)\mathbf{e}_\theta}{h(\theta, E_k)}, \tag{16}$$

and the in-plane normal unit vector is defined as

$$\mathbf{e}_x = \frac{r_0(\theta, E_k)\mathbf{e}_r - r_0'(\theta, E_k)\mathbf{e}_\theta}{h(\theta, E_k)}. \tag{17}$$

Together with the vertical unit vector $\mathbf{e}_z$, these vectors form a local orthonormal basis, where $\mathbf{e}_s$ is longitudinal and $\mathbf{e}_x$ and $\mathbf{e}_z$ are transverse. The in-plane transverse direction $\mathbf{e}_x$ reduces approximately to the global radial direction only when $|r_0'| \ll r_0$.

Since the reference closed orbit depends on energy, and its tangent and normal directions vary with azimuth, the local basis is both energy dependent and azimuth dependent. Therefore, for each particle, a reference point must first be identified on the interpolated closed orbit. The local coordinate system used for the particle is then constructed from the geometrical basis at that reference point.

### B. Construction of the local reference point and transverse coordinate

After the reference closed orbit and its local geometrical basis have been defined, a local reference point must be assigned to each particle on the reference orbit. As illustrated in Fig. 2(b), a straightforward choice would be the closed-orbit point $\mathbf{R}_0(\theta_p)$ at the same azimuth as the particle. This choice, however, mainly measures the particle displacement as a global radial offset. In a scaling FFA, the local normal direction of the reference orbit is generally not aligned with the global radial direction. Therefore, the same-azimuth point does not in general provide a geometrically consistent reference for the local transverse displacement.

In this work, the local reference point is defined as the normal projection of the particle onto the reference closed orbit in the median plane. Let the azimuth of this projected point be denoted by $\theta^*$. For a particle with cylindrical coordinates $(r_p, \theta_p, z_p)$, only its median-plane projection is used to determine the reference point, while the vertical coordinate $z_p$ is retained as the second transverse coordinate. The projected azimuth $\theta^*$ satisfies the orthogonality condition

$$[\mathbf{R}_p - \mathbf{R}_0(\theta^*)] \cdot \mathbf{e}_s(\theta^*) = 0, \tag{18}$$

where $\mathbf{R}_p$ denotes the median-plane projection of the particle position, $\mathbf{R}_0(\theta)$ is the position vector of the reference closed orbit, and $\mathbf{e}_s(\theta)$ is the local tangential unit vector of the reference orbit. This condition states that the displacement from the reference point to the particle, projected onto the median plane, is perpendicular to the local tangent of the closed orbit. Thus, $\mathbf{R}_0(\theta^*)$ is the normal projection point rather than the same-azimuth point $\mathbf{R}_0(\theta_p)$.

Solving Eq. (18) exactly would generally require an iterative procedure. Since this operation must be repeated for a large number of particles in the space charge calculation, a noniterative first-order correction is adopted. Specifically, the orthogonality condition is linearized around the particle azimuth $\theta_p$ by writing $\theta^* = \theta_p + \delta\theta$. This gives

$$\theta^* \simeq \theta_p + \frac{[r_p - r_0(\theta_p)]r_0'(\theta_p)}{r_0^2(\theta_p) + [r_0'(\theta_p)]^2}. \tag{19}$$

Here and in the following, $r_0(\theta)$, $r_0'(\theta)$, and $h(\theta)$ denote quantities on the selected reference closed orbit.

Once $\theta^*$ has been obtained, the local basis at the projected point is evaluated from Eqs. (16) and (17) at $\theta = \theta^*$.

The local transverse coordinate of the particle is then defined as the projection of its median-plane displacement from the local reference point onto $\mathbf{e}_x$:

$$x = [\mathbf{R}_p - \mathbf{R}_0(\theta^*)] \cdot \mathbf{e}_x(\theta^*). \tag{20}$$

The implementation uses a two-stage construction. First, the common closed orbit at the bunch-mean energy is used to recover the continuous longitudinal coordinate and fix the slice indices. After the slices have been fixed, the mean kinetic energy of each slice is evaluated, and the closed-orbit position and local basis used in Eq. (20) are reinterpolated at that slice-mean energy. All particles in one slice therefore share a single reference orbit and transverse frame, while different slices may use different energy-dependent closed orbits. The particle position in the local transverse plane is represented by $(x, z)$, where $z$ is directly taken from the global vertical coordinate.

## IV. RECONSTRUCTION OF THE LONGITUDINAL COORDINATE

### A. Requirements and difficulties of longitudinal coordinate reconstruction

The longitudinal coordinate determines both the slicing and the line charge density. In the global cylindrical tracking variables, its natural precursor is the projected reference-point azimuth $\theta^*$, but this quantity is periodic and has no length dimension. It must therefore be unwrapped and mapped through the precomputed closed-orbit arc-length function to obtain a continuous coordinate along the local tangent.

This reconstruction is particularly important for multiturn injection. Neighboring particles may have azimuths differing by integer multiples of $2\pi$, whereas reducing all azimuths to $[0, 2\pi)$ can split a continuous bunch across the periodic boundary. The following procedure recovers the occupied continuous interval before defining the bunch length and slice boundaries.

### B. Recovery of the continuous longitudinal coordinate

After the reference-point azimuth $\theta_i^*$ has been obtained for each particle, it must be converted into an azimuthal coordinate that can describe the continuous longitudinal distribution of the bunch. In the implementation, the reference-point azimuth is first normalized to a single-turn interval by taking it modulo $2\pi$:

$$\bar{\theta}_i^* = \theta_i^* \bmod 2\pi, \qquad \bar{\theta}_i^* \in [0, 2\pi). \tag{21}$$

This step places the reference-point azimuth within one turn, but it does not remove the discontinuity introduced by the periodic boundary. When a bunch crosses the boundary between 0 and $2\pi$, the single-turn representation still splits an otherwise continuous distribution into two parts. A range obtained directly from the minimum and maximum particle azimuths can then approach a full turn and is also sensitive to a small number of remote halo particles.

The occupied longitudinal intervals are therefore determined from bins of the periodic longitudinal density rather than directly from the outermost particle coordinates. As illustrated in Fig. 3, the smoothed density distribution is first used to distinguish continuous bunch regions from longitudinal halos. The latter do not independently determine the interval boundaries, but the corresponding particles are retained for the subsequent space charge calculation.

Low-density gaps between the bunch regions are then identified. The widest gap defines a common periodic cut. For $h = 1$, shifting the origin to this cut is sufficient to recover a single continuous bunch. For $h > 1$, the remaining gaps define the boundaries between the occupied rf buckets. All particles are unwrapped with the same common cut,

$$u_i = (\bar{\theta}_i^* - \theta_{\mathrm{cut}}) \bmod 2\pi, \quad u_i \in [0, 2\pi), \tag{22}$$

so that each occupied bucket forms a continuous bunch interval while the relative spacing between bunches is preserved.

Within each bunch interval, the main slicing range is determined from the density bins that together contain a prescribed fraction $q$ of the bunch charge. The calculation presented here uses $q = 0.995$. The outer boundaries of these bins define a continuous main range, including any internal low-density valleys. Particles ahead of or behind this range are assigned to a head or tail edge slice, respectively. They are not discarded and continue to participate in charge deposition, field solution, and field interpolation. Thus, a few remote particles do not enlarge all regular slices, while their space charge contribution is retained.

Finally, the unwrapped azimuth is converted to a longitudinal distance using the precomputed closed-orbit arc-length function. The transverse Poisson problem is solved independently in each longitudinal slice, whereas the longitudinal field is constructed from all slices belonging to the same bunch and is evaluated separately for each bunch.

The $h > 1$ procedure described above is a geometrical generalization of the longitudinal construction. The production benchmarks reported in this paper use $h = 1$.

## V. 2.5D SPACE CHARGE SOLVER IN THE LOCAL COORDINATE SYSTEM

### A. Transverse charge deposition and two-dimensional Poisson solve

In the reconstructed local coordinate system, the space charge field is calculated using a 2.5D slice-based model. The bunch is divided into a series of slices along the

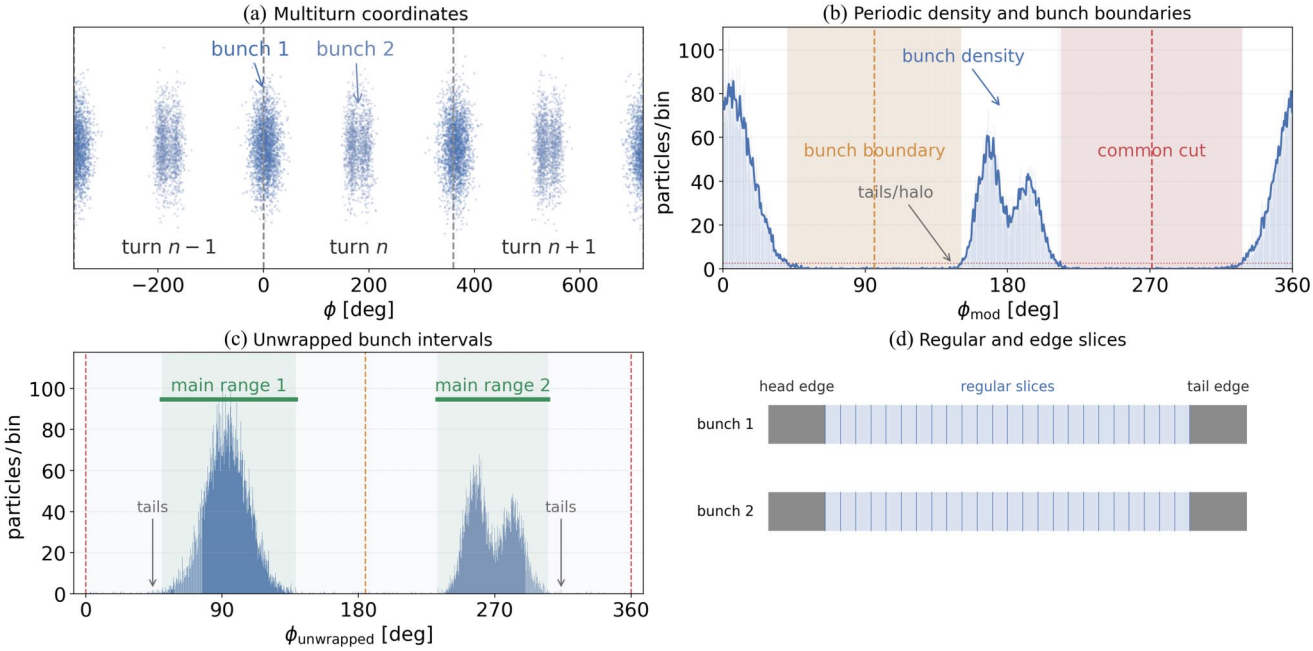



FIG. 3. Reconstruction of the continuous longitudinal coordinate. (a) Particle distribution in the multiturn azimuthal coordinate. (b) Periodic density distribution, identification of the bunch regions without allowing sparse halos to determine their boundaries, and selection of the common cut and bunch boundary from the low-density gaps. (c) Unwrapped bunch intervals and the main slicing range determined separately for each bunch. (d) Retention of particles outside the main ranges in the head and tail edge slices. All particles remain in the space charge calculation.

longitudinal coordinate $s$, and a 2D Poisson problem is solved in the local transverse plane $(x, z)$ of each slice. The resulting fields $E_x$ and $E_z$ represent the transverse components of the space charge field within the slice. The longitudinal field $E_s$ is constructed separately from the line charge density along $s$.

Let $L_b$ be the bunch length in the continuous longitudinal coordinate and $N_s$ be the number of longitudinal slices. The effective slice length is defined as

$$\Delta s_{\mathrm{eff}} = \frac{L_b}{N_s}. \tag{23}$$

For a macroparticle $p$ in the $k$th slice, its charge $q_p$ is distributed over the slice length and deposited onto the local transverse grid using the cloud-in-cell scheme, in which the particle charge is shared among the four neighboring transverse grid nodes using bilinear weights determined by its position within the cell. If $W_{ij}^{(p)}$ denotes the deposition weight of particle $p$ on the transverse grid node $(i, j)$, the discrete charge density in the slice is defined as

$$\rho_{k,ij} = \sum_{p \in k} \frac{q_p}{\Delta s_{\mathrm{eff}}\, \Delta x\, \Delta z} W_{ij}^{(p)}. \tag{24}$$

Here, $\rho_{k,ij}$ represents the charge density assigned to the transverse grid node $(x_i, z_j)$ in the $k$th slice, with units of $\mathrm{C/m^3}$. The corresponding line charge density in the slice is recovered by integrating over the transverse plane,

$$\lambda_k = \sum_{i,j} \rho_{k,ij}\, \Delta x\, \Delta z. \tag{25}$$

For open boundary conditions, the free-space Green's function of the two-dimensional Poisson equation can be written, up to an arbitrary additive constant, as

$$G(x, z) = -\frac{1}{2\pi\epsilon_0} \ln \sqrt{x^2 + z^2}. \tag{26}$$

The transverse electrostatic potential in the $k$th slice is obtained from the Green's-function convolution

$$\Phi_k(x_i, z_j) = \sum_{i', j'} G(x_i - x_{i'}, z_j - z_{j'}) \rho_{k,i'j'} \Delta x\, \Delta z. \tag{27}$$

This expression is the discrete form of the continuous convolution between the 2D Green's function and the transverse charge density in the slice.

Since the 2D Green's function has a logarithmic singularity at the source point, the self term is regularized numerically by replacing the zero distance with an equivalent radius related to the grid size. In this implementation, the equivalent radius is chosen as

$$r_{\mathrm{eq}} = \frac{1}{2}\sqrt{\Delta x^2 + \Delta z^2}. \tag{28}$$

A direct evaluation of Eq. (27) requires summing the contributions from all source points for each field point, with a computational complexity of $O(N_x^2 N_z^2)$ for a transverse grid of size $N_x \times N_z$. To improve computational efficiency, a zero-padded FFT-based fast convolution method is used. Specifically, the charge density and the Green's-function kernel are extended to a computational domain of size $2N_x \times 2N_z$, and the convolution is evaluated in this extended domain using FFTs:

$$\Phi_k = \mathcal{F}^{-1}[\mathcal{F}(\rho_k)\mathcal{F}(G)]\Delta x\,\Delta z, \tag{29}$$

where $\mathcal{F}$ and $\mathcal{F}^{-1}$ denote the 2D FFT and its inverse, respectively. The purpose of zero padding is to convert the periodic convolution inherent in FFTs into the linear convolution required in the physical domain. This avoids wrap-around errors associated with periodic convolution and preserves the physical meaning of the open-boundary Green's function. After the inverse transform, the original physical region of size $N_x \times N_z$ is extracted from the extended domain to obtain the transverse electrostatic potential in the slice.

Finally, the transverse and vertical electric fields in the slice are obtained from the negative gradient of the electrostatic potential:

$$E_{x,k} = -\frac{\partial \Phi_k}{\partial x}, \qquad E_{z,k} = -\frac{\partial \Phi_k}{\partial z}. \tag{30}$$

With the fast convolution method, the complexity of the potential solve for a single slice is reduced to $O[N_x N_z \log(N_x N_z)]$, which substantially improves the efficiency of the multislice 2.5D space charge field calculation.

### B. Longitudinal field approximation based on the line charge density

In the present 2.5D framework, the longitudinal field $E_s$ is approximated from the line charge density along the continuous longitudinal coordinate.

Let $\lambda(s)$ be the line charge density of the bunch along the continuous longitudinal coordinate $s$. The longitudinal electric field is written as a one-dimensional convolution,

$$E_s(s) = \int \lambda(s')K_s(s - s')ds', \tag{31}$$

where $K_s$ accounts for the finite transverse extent of the bunch, and its form depends on the assumed transverse charge distribution. For example, for a uniformly charged disk of radius $a$, the kernel is

$$K_{s,\mathrm{disk}}(\xi) = \frac{\mathrm{sgn}(\xi)}{2\pi\epsilon_0 a^2}\left(1 - \frac{|\xi|}{\sqrt{\xi^2 + a^2}}\right), \tag{32}$$

where $\xi = s - s'$ is the longitudinal separation. For a cylindrically symmetric Gaussian transverse distribution with rms size $\sigma_\perp$, the corresponding kernel is

$$K_{s,\mathrm{G}}(\xi) = \frac{\mathrm{sgn}(\xi)}{4\pi\epsilon_0\sigma_\perp^2}\left[1 - \sqrt{\pi}\,x\exp(x^2)\mathrm{erfc}(x)\right]. \tag{33}$$

Here, $x = |\xi|/(\sqrt{2}\sigma_\perp)$. At large longitudinal separation, these expressions recover the point-charge limit, while the near field retains the dependence on the transverse charge distribution.

In the discrete implementation, the line charge density is constructed from the total charge in each longitudinal slice. If the total charge in the $k$th slice is

$$Q_k = \sum_{p \in k} q_p,$$

then the slice-averaged line charge density is

$$\lambda_k = \frac{Q_k}{\Delta s_{\mathrm{eff}}}. \tag{34}$$

The longitudinal field on the slice grid is then evaluated as the discrete convolution

$$E_{s,k} = \sum_l \lambda_l K_s(s_k - s_l)\Delta s_{\mathrm{eff}}. \tag{35}$$

The resulting field can be assigned to the slice centers or interpolated to the longitudinal positions of individual particles.

### C. Back-projection of the local field and relativistic reduction

The local space charge field obtained on the slice grid must be interpolated back to the particle position and transformed into global cylindrical components for particle pushing. For each particle, the code first interpolates $E_x$ and $E_z$ from the local transverse grid according to its slice index and local transverse coordinates $(x, z)$, and obtains $E_s$ from its longitudinal position. The local electrostatic space charge field at the particle position can be written as

$$\mathbf{E}_{\mathrm{loc}} = E_x\mathbf{e}_x + E_s\mathbf{e}_s + E_z\mathbf{e}_z. \tag{36}$$

Here, $\mathbf{e}_x$ is the local normal unit vector in the median plane, $\mathbf{e}_s$ is the local tangential unit vector along the reference closed orbit, and $\mathbf{e}_z$ is the vertical unit vector. These local basis vectors have been defined previously

from the reference-orbit geometry and are evaluated at the projected reference point $\theta^*$ of the particle.

Within the local 2.5D and quasistatic approximation, the transverse fields $E_x$ and $E_z$ are obtained from the transverse 2D Poisson equation. For a relativistic beam, the self-magnetic field associated with the transverse electric self-field partially cancels the transverse Lorentz force. The leading transverse space charge force is therefore reduced by a factor $1/\gamma^2$, where $\gamma$ is the relativistic factor of the particle. In the particle pusher, this effect is represented by the effective transverse field components

$$E_{x,\mathrm{eff}} = \frac{E_x}{\gamma^2},$$
$$E_{z,\mathrm{eff}} = \frac{E_z}{\gamma^2}. \tag{37}$$

These effective fields do not redefine the electrostatic field obtained from the Poisson solve. They are used only to represent the leading cancellation between the electric and magnetic self-forces in the transverse Lorentz force.

The longitudinal component $E_s$ is taken from the one-dimensional line-charge model described in the previous subsection and is applied directly along the local longitudinal direction. This is because the magnetic self-field does not produce an analogous longitudinal Lorentz-force cancellation. The present treatment should therefore be regarded as an approximate longitudinal self-field model, while the dominant transverse space charge force is corrected by the usual relativistic reduction factor.

The effective local space charge field used for particle pushing is therefore

$$\mathbf{E}_{\mathrm{loc,eff}} = E_{x,\mathrm{eff}}\mathbf{e}_x + E_s\mathbf{e}_s + E_{z,\mathrm{eff}}\mathbf{e}_z. \tag{38}$$

Since an FFA closed orbit is generally not a constant-radius circular orbit, the local tangential and normal directions usually contain both global radial and azimuthal components. Expanding Eq. (38) in the global cylindrical basis gives

$$\mathbf{E}_{\mathrm{glob,eff}} = E_r\mathbf{e}_r + E_\theta\mathbf{e}_\theta + E_z^{\mathrm{glob}}\mathbf{e}_z. \tag{39}$$

Using the relation between the local basis and the cylindrical basis, one obtains

$$\begin{pmatrix} E_r \\ E_\theta \end{pmatrix} = \frac{1}{h(\theta^*)} \begin{pmatrix} r_0(\theta^*) & r_0'(\theta^*) \\ -r_0'(\theta^*) & r_0(\theta^*) \end{pmatrix} \begin{pmatrix} E_{x,\mathrm{eff}} \\ E_s \end{pmatrix}, \tag{40}$$

while the vertical component is

$$E_z^{\mathrm{glob}} = E_{z,\mathrm{eff}}. \tag{41}$$

Equation (40) shows that the local transverse and longitudinal fields generally both contribute to the global radial and azimuthal components after back-projection.

## VI. BENCHMARK VALIDATION AND APPLICATION

### A. Benchmark of the transverse space charge field

To validate the transverse field calculation in the proposed 2.5D space charge model, a long arc-shaped test bunch is constructed along the reference closed orbit, and the numerical fields obtained from the 2.5D solver are compared with analytical reference solutions in selected local slices.

We first examine the transverse space charge field. A Gaussian bunch is generated along the closed orbit. In each longitudinal slice, the transverse distribution is assumed to be cylindrically symmetric in the local transverse plane, with an rms size $\sigma$. The longitudinal distribution is also taken to be Gaussian, so that different slices have different line charge densities. For the $k$th longitudinal slice, the slice-averaged line charge density is denoted by $\lambda_k$. In the local transverse plane $(x, z)$, where $x$ is the local horizontal transverse coordinate and $z$ is the vertical coordinate, the transverse Gaussian distribution of this slice is written as

$$\rho_k(x,z) = \frac{\lambda_k}{2\pi\sigma^2}\exp\left[-\frac{x^2+z^2}{2\sigma^2}\right]. \tag{42}$$

Here, $\rho_k(x, z)$ represents the volume charge density, so that its integral over the transverse plane gives $\lambda_k$.

For a locally straight, infinitely long Gaussian line-charge distribution, the analytical radial electric field in the transverse plane is

$$E_u(u) = \frac{\lambda_k}{2\pi\epsilon_0 u}\left[1-\exp\left(-\frac{u^2}{2\sigma^2}\right)\right], \quad u = \sqrt{x^2+z^2}. \tag{43}$$

The corresponding field components in the local horizontal and vertical directions are

$$E_x(x,z) = E_u(u)\frac{x}{u}, \qquad E_z(x,z) = E_u(u)\frac{z}{u}. \tag{44}$$

At $u = 0$, the field is evaluated by its limiting value, which is zero by symmetry.

In the present benchmark, the numerical transverse field is compared with the analytical field after applying the same relativistic reduction used in the particle pusher. Therefore, the effective analytical radial field is

$$E_{u,\mathrm{eff}}(u) = \frac{1}{\gamma^2}\frac{\lambda_k}{2\pi\epsilon_0 u}\left[1-\exp\left(-\frac{u^2}{2\sigma^2}\right)\right], \tag{45}$$

where $\gamma$ is the relativistic Lorentz factor of the beam particles. The corresponding effective transverse field components are obtained from Eq. (44) by replacing $E_u$ with $E_{u,\mathrm{eff}}$.

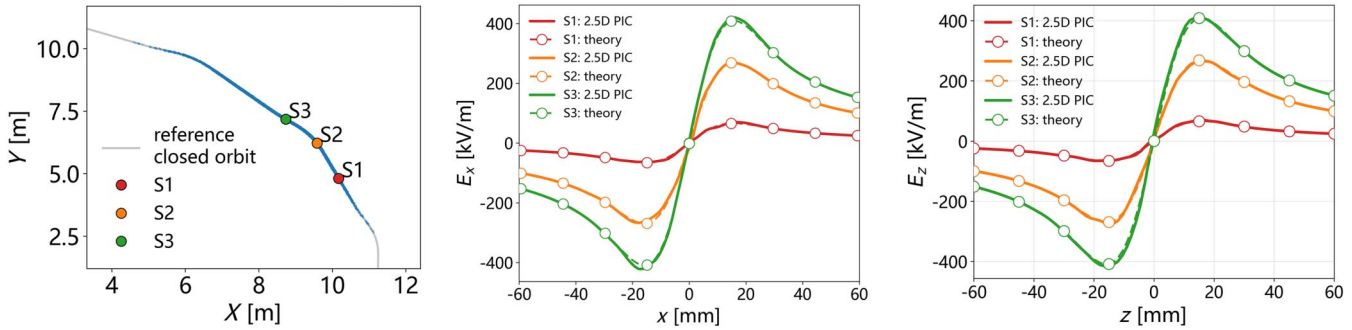



FIG. 4. Benchmark of the 2.5D space charge field calculation for a long arc-shaped Gaussian bunch. The left panel shows selected longitudinal slices along the reference closed orbit. The middle panel compares the numerical and analytical $E_x$ profiles on the horizontal midplane $z = 0$. The right panel compares the numerical and analytical $E_z$ profiles on the vertical axis $x = 0$.

The 2.5D space charge solver is applied to the entire long arc-shaped Gaussian bunch. This gives the local transverse field distributions $E_x(x, z; s_k)$ and $E_z(x, z; s_k)$ for each longitudinal slice. Several representative slices are selected along the bunch, as shown in the left panel of Fig. 4. For each selected slice, the field profile on the horizontal midplane, $E_x(x, z = 0; s_k)$, and that on the vertical axis, $E_z(x = 0, z; s_k)$, are extracted and compared with the analytical Gaussian field determined by the corresponding line charge density $\lambda_k$.

The comparison in the middle and right panels of Fig. 4 shows that the numerical fields agree well with the analytical solutions for all selected slices. Slices near the bunch center have larger $\lambda_k$ and therefore produce stronger transverse fields, whereas slices away from the bunch center have smaller line charge densities and correspondingly weaker fields. We define the relative rms error as

$$\epsilon_{\mathrm{rms}} = \left[\frac{\sum_m (E_m^{\mathrm{num}} - E_m^{\mathrm{ref}})^2}{\sum_m (E_m^{\mathrm{ref}})^2}\right]^{1/2}. \tag{46}$$

For the selected slices, the relative rms discrepancies of the $E_z$ profiles are 4.44%, 2.27%, and 3.51%, respectively.

### B. Benchmark of the longitudinal space charge field

An axisymmetric Gaussian bunch is used to benchmark the longitudinal electric field on the bunch axis. Let the bunch center be located at $s_c$, the longitudinal rms length be $\sigma_s$, the transverse rms size be $\sigma_\perp$, and the total charge be $Q$. The 3D charge density is written as

$$\rho(u, s) = \frac{Q}{(2\pi)^{3/2}\sigma_\perp^2 \sigma_s} \exp\left[-\frac{u^2}{2\sigma_\perp^2} - \frac{(s - s_c)^2}{2\sigma_s^2}\right], \tag{47}$$

where $u$ is the transverse radius with respect to the bunch axis, and $s$ is the longitudinal coordinate along the bunch.

For this axisymmetric Gaussian charge distribution, the longitudinal electric field on the bunch axis can be expressed as

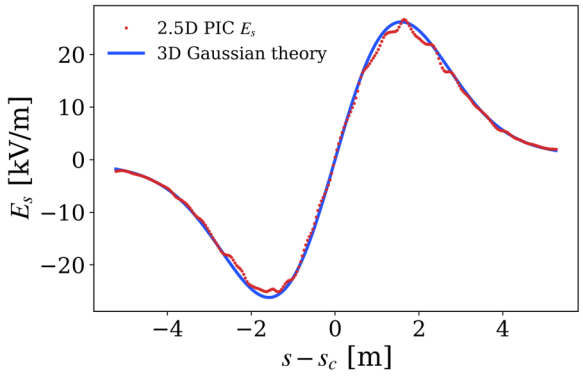



FIG. 5. On-axis longitudinal electric field of a 3D Gaussian bunch. The analytical result is compared with the longitudinal field calculated by the 2.5D PIC model using a Gaussian transverse kernel.

$$E_{s,\mathrm{th}}(s) = \frac{Q}{4\pi\epsilon_0} \frac{s - s_c}{\sqrt{2\pi}} \int_0^\infty \frac{\exp\left[-\frac{(s-s_c)^2}{2(\sigma_s^2+\tau)}\right]}{(\sigma_\perp^2 + \tau)(\sigma_s^2 + \tau)^{3/2}}\, d\tau. \tag{48}$$

Here, $\tau$ is an auxiliary integration variable with the dimension of length squared.

Figure 5 compares Eq. (48) with the numerical field obtained using a Gaussian kernel and a smoothed sampled line charge density. The rms difference normalized to the theoretical peak field is 2.9%, and the numerical peak is higher than the analytical result by 1.8%.

### C. Benchmark of tune shift

Using the lattice and numerical setup described in the Appendix, we first examine the transverse tune shift, one of the most direct dynamical measures of space charge effects [21,22]. Two representative beam distributions are considered in this benchmark. The first is a beam with a transverse KV distribution and a longitudinal Gaussian

line charge density. This case is used to validate the linear space charge tune shift, because the transverse space charge field of a KV beam is linear in the beam core. The second is a beam with a transverse Gaussian distribution and a longitudinally uniform line charge density. This case is used to validate the nonlinear tune footprint, because the transverse Gaussian field depends on particle amplitude. The theoretical results obtained for these two cases are compared with the tunes extracted from the 2.5D PIC tracking.

In the absence of space charge, the transverse linear equations of motion are

$$x'' + K_x(s)x = 0 \tag{49}$$

and

$$z'' + K_z(s)z = 0, \tag{50}$$

where $s$ is the arc-length coordinate along the reference orbit, and $K_x(s)$ and $K_z(s)$ are the external linear focusing functions of the lattice. When the space charge force is linearized near the beam center, the equations become

$$x'' + [K_x(s) + k_{\mathrm{sc},x}(s)]x = 0 \tag{51}$$

and

$$z'' + [K_z(s) + k_{\mathrm{sc},z}(s)]z = 0. \tag{52}$$

The corresponding tune shifts are

$$\Delta Q_x = \frac{1}{4\pi}\int_0^C \beta_x(s)k_{\mathrm{sc},x}(s)ds \tag{53}$$

and

$$\Delta Q_z = \frac{1}{4\pi}\int_0^C \beta_z(s)k_{\mathrm{sc},z}(s)ds, \tag{54}$$

where $C$ is the ring circumference, and $\beta_x(s)$ and $\beta_z(s)$ are the zero-current beta functions. For later comparison, the depressed tune in either transverse plane is written as $Q_u = Q_{u0} + \Delta Q_u$, and the corresponding tune-depression ratio is $\eta_u = Q_u/Q_{u0}$, where $u = x, z$ and $Q_{u0}$ is the zero-current tune. Under the near-axis approximation, the space charge focusing terms are written as

$$k_{\mathrm{sc},x}(s) = -\frac{q}{m\beta^2\gamma^3c^2}\frac{E_x}{x}(s) \tag{55}$$

and

$$k_{\mathrm{sc},z}(s) = -\frac{q}{m\beta^2\gamma^3c^2}\frac{E_z}{z}(s). \tag{56}$$

Here, $E_x$ and $E_z$ denote the electrostatic fields generated by the transverse charge distribution. The factor $1/(\beta^2\gamma^3)$ results from the relativistic transverse space charge force reduction together with the conversion from force to transverse curvature with respect to the arc-length variable.

For the first benchmark, the beam is assumed to have a transverse KV distribution and a longitudinal Gaussian line charge density. In this case, the transverse space charge field is linear, while the longitudinal variation enters through the local line charge density $\lambda_q(s)$. If the rms beam sizes are denoted by $\sigma_x$ and $\sigma_z$, the field gradients are written as

$$\frac{E_x}{x} = \frac{\lambda_q(s)}{4\pi\epsilon_0\,\sigma_x(s)[\sigma_x(s) + \sigma_z(s)]} \tag{57}$$

and

$$\frac{E_z}{z} = \frac{\lambda_q(s)}{4\pi\epsilon_0\,\sigma_z(s)[\sigma_x(s) + \sigma_z(s)]}. \tag{58}$$

The rms beam sizes are evaluated from the zero-current Twiss functions,

$$\sigma_x^2(s) = \beta_x(s)\epsilon_{x,\mathrm{rms}} \tag{59}$$

and

$$\sigma_z^2(s) = \beta_z(s)\epsilon_{z,\mathrm{rms}}. \tag{60}$$

For the longitudinal Gaussian distribution, the line charge density is

$$\lambda_q(s) = \frac{Q}{\sqrt{2\pi}\sigma_s}\exp\left[-\frac{(s - s_c)^2}{2\sigma_s^2}\right], \tag{61}$$

where $Q$ is the total bunch charge, $s_c$ is the bunch center, and $\sigma_s$ is the longitudinal rms bunch length. For given $\lambda_q(s)$, $\beta_x(s)$, $\beta_z(s)$, and transverse emittances, Eqs. (53)–(61) give the theoretical incoherent tune shifts for the KV beam.

For the second benchmark, the beam is assumed to have a transverse Gaussian distribution and a longitudinally uniform line charge density. In this case, the line charge density is constant along the bunch,

$$\lambda_q = \frac{N_p e}{L_b}, \tag{62}$$

where $N_p$ is the total number of protons in the bunch, $e$ is the elementary charge, and $L_b$ is the bunch length. For a

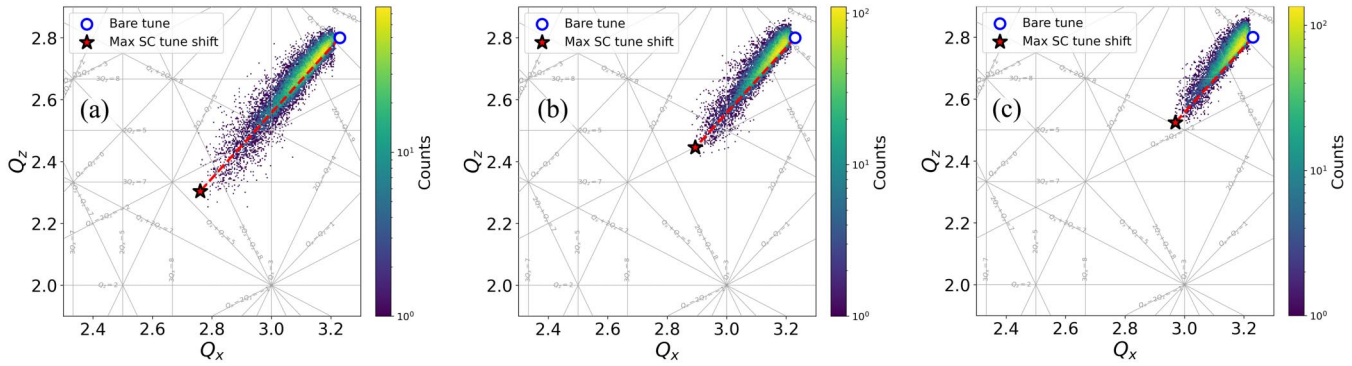



FIG. 6. Benchmark of the 2.5D space charge tune shift for beams with transverse KV distributions and longitudinal Gaussian line charge densities. The panels correspond to transverse rms emittances of (a) $\epsilon = 50\pi$ mm mrad, (b) $\epsilon = 70\pi$ mm mrad, and (c) $\epsilon = 90\pi$ mm mrad. The blue circle denotes the bare tune, the red star denotes the theoretical core tune with the maximum space charge tune shift, and the dashed red line shows the analytical KV-Gaussian tune spread direction. The gray lines show nearby resonance conditions. As the emittance increases, the space charge tune shift decreases, and the tune distribution moves closer to the bare tune.

cylindrically symmetric transverse Gaussian distribution with rms size $\sigma_\perp$, the volume charge density is

$$\rho(u) = \frac{\lambda_q}{2\pi\sigma_\perp^2}\exp\left(-\frac{u^2}{2\sigma_\perp^2}\right), \tag{63}$$

where

$$u^2 = x^2 + z^2. \tag{64}$$

The corresponding radial electric field is

$$E_u(u) = \frac{\lambda_q}{2\pi\epsilon_0 u}\left[1 - \exp\left(-\frac{u^2}{2\sigma_\perp^2}\right)\right]. \tag{65}$$

The transverse field components are then

$$E_x = E_u(u)\frac{x}{u} \tag{66}$$

and

$$E_z = E_u(u)\frac{z}{u}. \tag{67}$$

Although the Gaussian field can be linearized near the bunch center, it has a clear amplitude dependence at finite transverse amplitudes. Therefore, the Gaussian benchmark is performed by directly integrating the transverse Hill equations with nonlinear space charge terms:

$$x'' + K_x(s)x = \frac{q}{\gamma^3 m\beta^2 c^2}E_x(x, z; s) \tag{68}$$

and

$$z'' + K_z(s)z = \frac{q}{\gamma^3 m\beta^2 c^2}E_z(x, z; s). \tag{69}$$

Here, $E_x(x, z; s)$ and $E_z(x, z; s)$ are evaluated from the local Gaussian beam sizes. The local rms beam sizes are again determined from Eqs. (59) and (60).

In the theoretical calculation of the Gaussian tune footprint, the same transverse amplitudes as those of the PyFFA tracking particles are used as initial conditions. The nonlinear Hill equations are then integrated with high numerical accuracy to obtain the turn-by-turn transverse motion of each particle. A spectral analysis is applied to the $x$ and $z$ oscillation signals to extract the corresponding tunes $Q_x$ and $Q_z$. The result is therefore a theoretical tune spread that includes the amplitude dependence of the transverse Gaussian space charge field.

The theoretical tune spreads are compared with the 2.5D PIC tracking results in Figs. 6 and 7. For the beam with a transverse KV distribution and a longitudinal Gaussian line charge density, the analytical model predicts an approximately straight tune-shift line in the $(Q_x, Q_z)$ plane, as shown in Fig. 6. This line describes the slice-dependent linear space charge defocusing. The PIC tune distributions follow this predicted direction, while some large-amplitude particles extend above the line because the nonlinear lattice tune shift increases $Q_z$, producing a triangular-like spread. Using the zero-current tunes $(Q_{x0}, Q_{z0}) = (3.233, 2.813)$, the PIC results for the 50, 70, and 90 $\pi$ mm mrad cases give $Q_x = 2.7417$, 2.8825, and 2.9694, while the corresponding analytical values are $Q_x = 2.7631$, 2.8974, and 2.9719. The PIC tune-depression ratios $Q_x/Q_{x0}$ are 0.848, 0.892, and 0.918, compared with the analytical values of 0.855, 0.896, and 0.919, respectively. The PIC and analytical results therefore agree closely over the full emittance range. A somewhat larger deviation is observed in the vertical direction, mainly

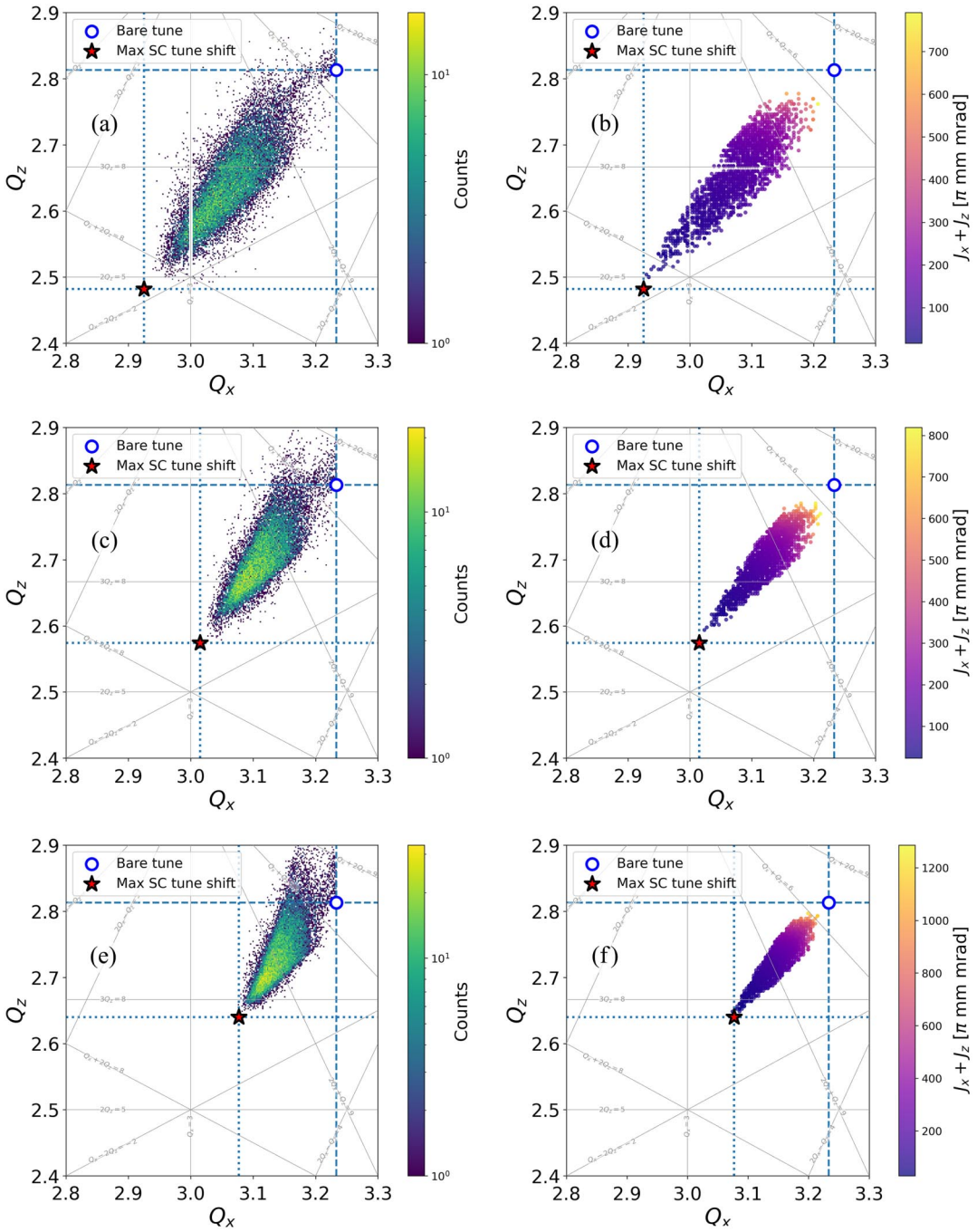



FIG. 7. Tune-spread benchmark for beams with transverse Gaussian distributions and longitudinally uniform line charge densities. The left column shows the tune spreads obtained from 2.5D PIC tracking, while the right column shows the corresponding tune spreads obtained from theoretical solutions with the same transverse amplitude range. The panels correspond to (a),(b) $\epsilon = 40\pi$ mm mrad, (c),(d) $\epsilon = 60\pi$ mm mrad, and (e),(f) $\epsilon = 80\pi$ mm mrad. Panels (a),(c),(e) show the PIC tracking results, and panels (b),(d),(f) show the analytical theory. In the PIC results, the color represents particle counts; in the theoretical results, the color represents the transverse action $J_x + J_z$. The blue circles and dashed lines indicate the bare tune, the red stars and dotted lines indicate the maximum space charge tune shift, and the gray lines show nearby resonances. As the emittance increases, the space charge tune shift decreases and the tune footprint moves closer to the bare tune.

attributed to the nonlinear lattice tune shifts, but this remains smaller than the overall vertical space charge tune-shift scale. As the transverse emittance increases, the overall space charge tune shift decreases and the tune distribution moves closer to the bare tune, consistent with the theoretical expectation.

For the beam with a transverse Gaussian distribution and a longitudinally uniform line charge density, the tune

spread obtained from PIC tracking shows good consistency with that obtained from nonlinear theoretical tracking, as shown in Fig. 7. The large tune-shift region is more densely populated because small-amplitude particles are concentrated near the Gaussian beam core and experience the strongest space charge defocusing. Particles with larger amplitudes sample the beam halo, where the average space charge force is weaker, and their tunes move toward the bare tune. As the transverse emittance increases, the beam size becomes larger, the space charge tune shift decreases, and the tune spread moves closer to the bare tune. For the 40, 60, and 80 $\pi$ mm mrad cases, the PIC results give $Q_x = 2.935$, 3.015, and 3.077, compared with the analytical values of $Q_x = 2.922$, 3.023, and 3.074. In the vertical direction, the PIC results are $Q_z = 2.478$, 2.575, and 2.643, while the analytical values are $Q_z = 2.477$, 2.594, and 2.645. The corresponding PIC tune-depression ratios $Q_x/Q_{x0}$ are 0.908, 0.933, and 0.952, compared with the analytical values of 0.904, 0.935, and 0.951. For $Q_z/Q_{z0}$, the PIC ratios are 0.881, 0.915, and 0.940, while the analytical values are 0.881, 0.922, and 0.940. The small differences relative to the overall space charge tune-shift scale show that the predicted tune spread and its emittance dependence are reproduced reasonably well.

### D. rms envelope benchmark for beam size evolution

In addition to the tune-shift benchmark, the rms envelope equation [23] is used to validate the beam-size evolution obtained from PyFFA tracking. In typical parameter regimes, the beam envelope is mainly governed by the external focusing lattice, and the additional effect of space charge may be modest over a short distance. To make the space charge contribution clearly visible in this benchmark, a relatively high beam intensity is used so that the envelope evolution is measurably modified by the space charge force.

For a KV beam, the transverse rms envelope equations can be written as

$$\sigma_x'' + K_x(s)\sigma_x - \frac{\epsilon_x^2}{\sigma_x^3} - \frac{K_{\mathrm{sc}}}{\sigma_x + \sigma_z} = 0 \tag{70}$$

and

$$\sigma_z'' + K_z(s)\sigma_z - \frac{\epsilon_z^2}{\sigma_z^3} - \frac{K_{\mathrm{sc}}}{\sigma_x + \sigma_z} = 0, \tag{71}$$

where $\sigma_x$ and $\sigma_z$ are the rms beam sizes in the two transverse directions, $K_x(s)$ and $K_z(s)$ are the external focusing functions reconstructed from the zero-current optics, $\epsilon_x$ and $\epsilon_z$ are the rms geometric emittances, and $K_{\mathrm{sc}}$ characterizes the space charge strength. For a longitudinally uniform bunch, $K_{\mathrm{sc}}$ is determined by the line charge density, beam energy, and particle species.

In this benchmark, the theoretical envelope equations are initialized with the same zero-current Twiss parameters as those used to generate the initial bunch in PyFFA. The initial rms beam sizes are

$$\sigma_x(0) = \sqrt{\beta_x(0)\epsilon_x} \tag{72}$$

and

$$\sigma_z(0) = \sqrt{\beta_z(0)\epsilon_z}. \tag{73}$$

The initial envelope slopes are determined from the corresponding Twiss $\alpha$ functions,

$$\sigma_x'(0) = -\frac{\alpha_x(0)\epsilon_x}{\sigma_x(0)} \tag{74}$$

and

$$\sigma_z'(0) = -\frac{\alpha_z(0)\epsilon_z}{\sigma_z(0)}. \tag{75}$$

The rms envelope equations are then integrated along the reference orbit using the same emittances, line charge density, beam energy, and space charge strength as those used in the PyFFA tracking.

In the PyFFA simulation, the rms beam sizes are calculated from the tracked particles at different azimuthal positions and compared with the envelope-equation solution.

As shown in Fig. 8, the blue curves represent the envelope-equation results, and the red stars represent the PyFFA tracking results. For both cases with and without space charge, the tracking results agree well with the theoretical envelope curves.

### E. Benchmark of longitudinal space charge effects

We next examine whether the longitudinal self-field model, once coupled to the complete FFA tracking framework, reproduces the expected longitudinal collective dynamics. Whereas the Gaussian analytical field benchmark in Sec. VI B tests the longitudinal electric-field calculation itself, the present comparison tests the longitudinal dynamical implementation and coupling consistency.

The benchmark uses the lattice and beam parameters summarized in Table I in the Appendix. The rf settings are $h = 1$ and $\varphi_s = 0$, corresponding to a stationary rf bucket. The initial longitudinal distribution is an elliptical waterbag, with particles uniformly distributed inside the ellipse in the $(\tau, \Delta E_k)$ phase plane. Two full PyFFA tracking simulations were performed using the same initial particle ensemble, lattice, rf parameters, and transverse

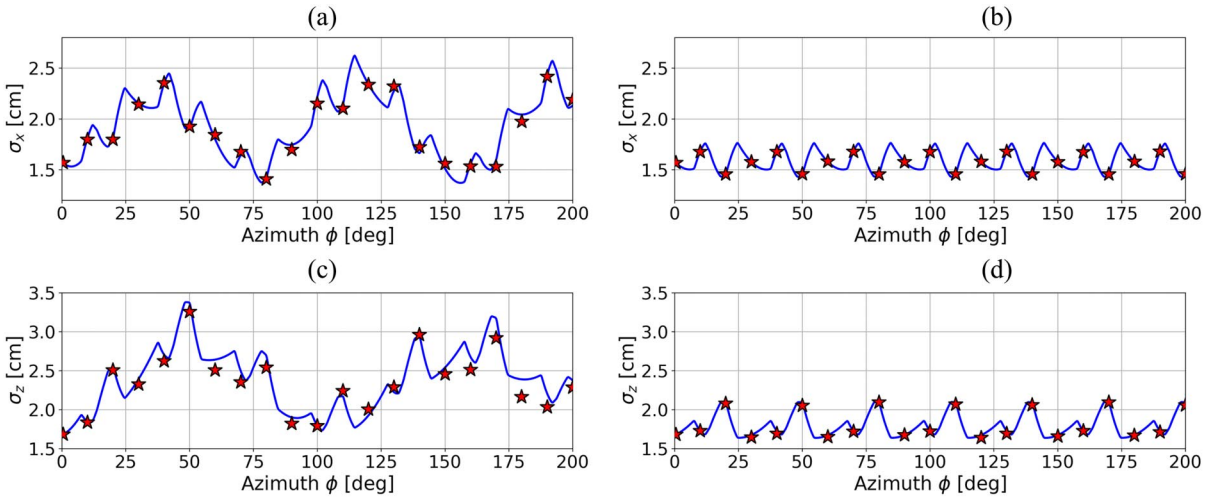



FIG. 8. Comparison of the horizontal and vertical rms beam-size evolution with and without space charge. Panels (a),(b) show $\sigma_x$ with and without space charge, respectively, while panels (c),(d) show the corresponding vertical quantity $\sigma_z$. The blue curves show the theoretical results obtained from the rms envelope equation, while the red stars show the rms beam sizes obtained from PyFFA particle tracking.

space-charge treatment, differing only in whether longitudinal space charge was included.

For comparison with the complete tracking calculation, the reduced 1D analytical model is constructed by retaining longitudinal slip, the rf kick, and the longitudinal space charge field while removing the transverse degrees of freedom. It therefore provides a reduced dynamical benchmark for the longitudinal implementation rather than an independent three-dimensional field solution. The complete PyFFA calculation uses the 2.5D self-field formulation described above. Let $\tau_i$ be the arrival-time deviation of the $i$th particle from the synchronous particle and let

$$\Delta E_{k,i} = E_{k,i} - E_{k0}, \tag{76}$$

where $E_{k0}$ is the synchronous kinetic energy. The corresponding longitudinal coordinate is

$$s_i = -v_0 \tau_i, \tag{77}$$

where $v_0 = \beta_0 c$ is the synchronous-particle velocity. The longitudinal equations of motion are

$$\frac{d\tau_i}{dt} = \frac{T(E_{k0} + \Delta E_{k,i}) - T_0}{T_0} \tag{78}$$

and

$$\frac{d\Delta E_{k,i}}{dt} = \frac{qV_{\mathrm{turn}}}{T_0}[\sin(\varphi_s + \omega_{\mathrm{rf}}\tau_i) - \sin\varphi_s] + qv_0 E_s(s_i, t). \tag{79}$$

Here, $T_0$ is the synchronous revolution period, $T(E_k)$ is the energy-dependent revolution period, $V_{\mathrm{turn}}$ is the total rf voltage per turn, $\varphi_s$ is the synchronous phase, and $\omega_{\mathrm{rf}}$ is the rf angular frequency. Equation (78) describes longitudinal slip arising from the energy dependence of the revolution period. Equation (79) includes both the rf energy gain and the work done by the longitudinal space charge field. The field $E_s(s,t)$ is evaluated from the instantaneous line charge density using Eqs. (31)–(35). The reduced 1D analytical model uses the same initial longitudinal distribution, rf parameters, and longitudinal field prescription as the complete tracking calculation, but does not include transverse motion. In the comparison without longitudinal space charge, $E_s$ is set to zero in both calculations.

Figures 9 and 10 compare complete PyFFA tracking with the reduced 1D analytical model at turns 1, 51, 101, 151, 201, and 251 with longitudinal space charge included and omitted, respectively. In the calculation without longitudinal space charge, the distribution remains approximately elliptical and exhibits only weak periodic breathing, indicating that the initial waterbag is approximately matched to the rf-only longitudinal dynamics. With longitudinal space charge included, the effective longitudinal focusing is modified and weakened, and the initial rf-only waterbag is no longer matched to the combined rf and space charge forces. This excites a coherent longitudinal mismatch oscillation, with pronounced periodic exchange between bunch length and energy spread. The reduced 1D analytical model reproduces both the coherent oscillation and the phase space shearing seen in complete PyFFA tracking.

For a quantitative comparison, the rms bunch length $\sigma_s$ and rms energy spread $\sigma_E$ are calculated at the selected turns. With longitudinal space charge included, the maximum relative differences between complete PyFFA tracking and the reduced 1D analytical model are 0.91%

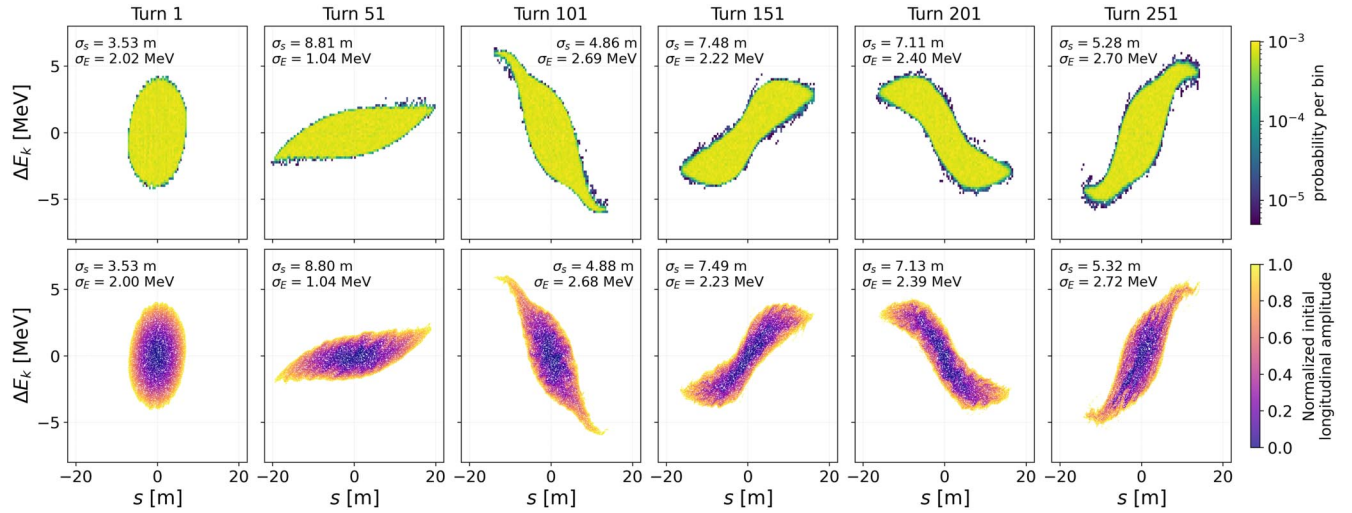



FIG. 9. Longitudinal phase-space evolution with longitudinal space charge included. The columns correspond to turns 1, 51, 101, 151, 201, and 251. The upper and lower rows show complete PyFFA tracking and the reduced 1D analytical model, respectively. The two color scales represent the probability per bin and the normalized initial longitudinal amplitude. The reduced 1D analytical model reproduces the coherent bunch-length oscillation, phase-space rotation, and shearing observed in complete PyFFA tracking.

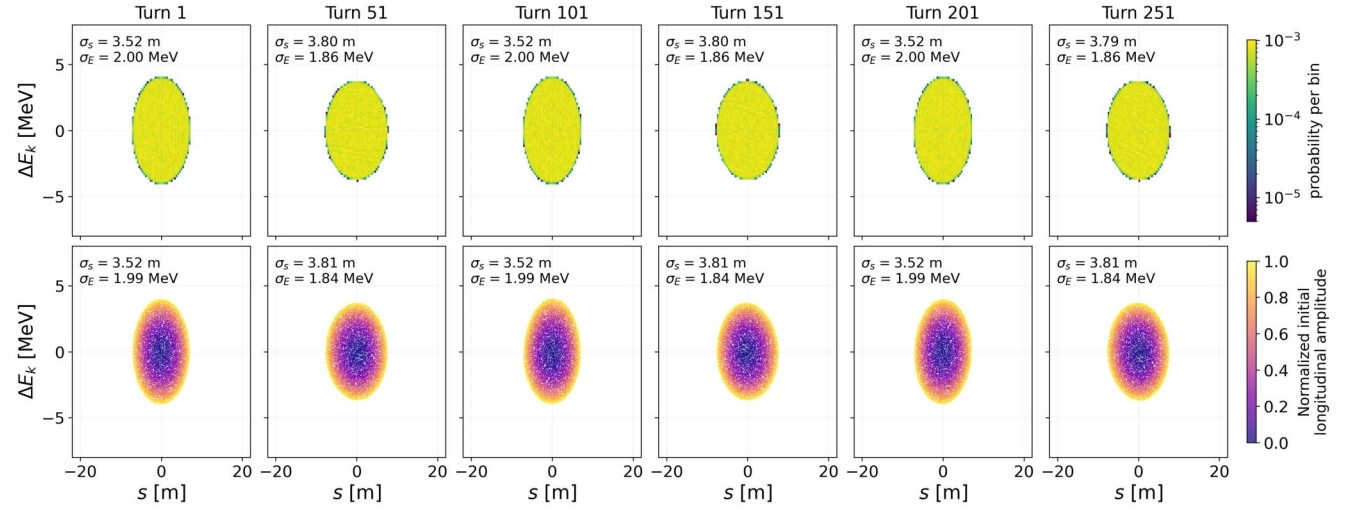



FIG. 10. Longitudinal phase-space evolution with longitudinal space charge omitted. The columns correspond to turns 1, 51, 101, 151, 201, and 251. The upper and lower rows show complete PyFFA tracking and the reduced 1D analytical model, respectively. The distribution remains approximately elliptical and exhibits only weak periodic breathing in both calculations.

for $\sigma_s$ and 1.40% for $\sigma_E$. With longitudinal space charge omitted, the corresponding differences are 0.43% and 1.08%. The agreement in both cases supports the consistency of the longitudinal dynamical implementation and its coupling to complete PyFFA tracking.

### F. Application

The proposed model has been implemented in the PyFFA tracking code and has been applied to preliminary beam dynamics studies of a high-intensity proton FFA accelerator scheme, referred to as CSNS/FFA, with an injection energy of 300 MeV and an extraction energy of 600 MeV.

In this high-intensity FFA design, the closed-orbit circumference increases from approximately 71.53 m at injection to 75.02 m at extraction, and the lattice consists of 16 periodic cells. The FFA receives a 300 MeV$H^-$ beam from the linac, and high-intensity beam accumulation is achieved through charge-exchange injection and transverse phase-space painting. The designed repetition rate is 25 Hz, with an average extracted beam power of

approximately 50 kW, corresponding to about $2.08 \times 10^{13}$ protons per bunch. In the present application, this particle number is used to characterize high intensity. As shown in Table II, the modeled bunch intensity is of the same order as those of representative high-intensity rapid-cycling synchrotrons.

Painting injection is applied for optimizing the phase-space distribution of the beam and mitigating space charge effects. Figure 11 shows the painting injection distributions obtained from PyFFA simulations, comparing the cases without space charge and with high-intensity space charge. Under the influence of strong space charge, the bunch distribution exhibits transverse broadening, density redistribution, and changes in phase-space structure, indicating that space charge can significantly affect the final beam distribution formed by painting injection under high-intensity conditions. The approximately square outer boundaries observed in both the space-charge and no-space-charge cases arise mainly from the linear painting curves used in the simulations.

In addition, Figs. 12 and 13 show the emittance evolution and space charge tune footprint obtained from PyFFA during the full 300–600 MeV acceleration process, respectively.

Further studies are currently underway on resonance crossing driven by space charge tune shift, the mechanism

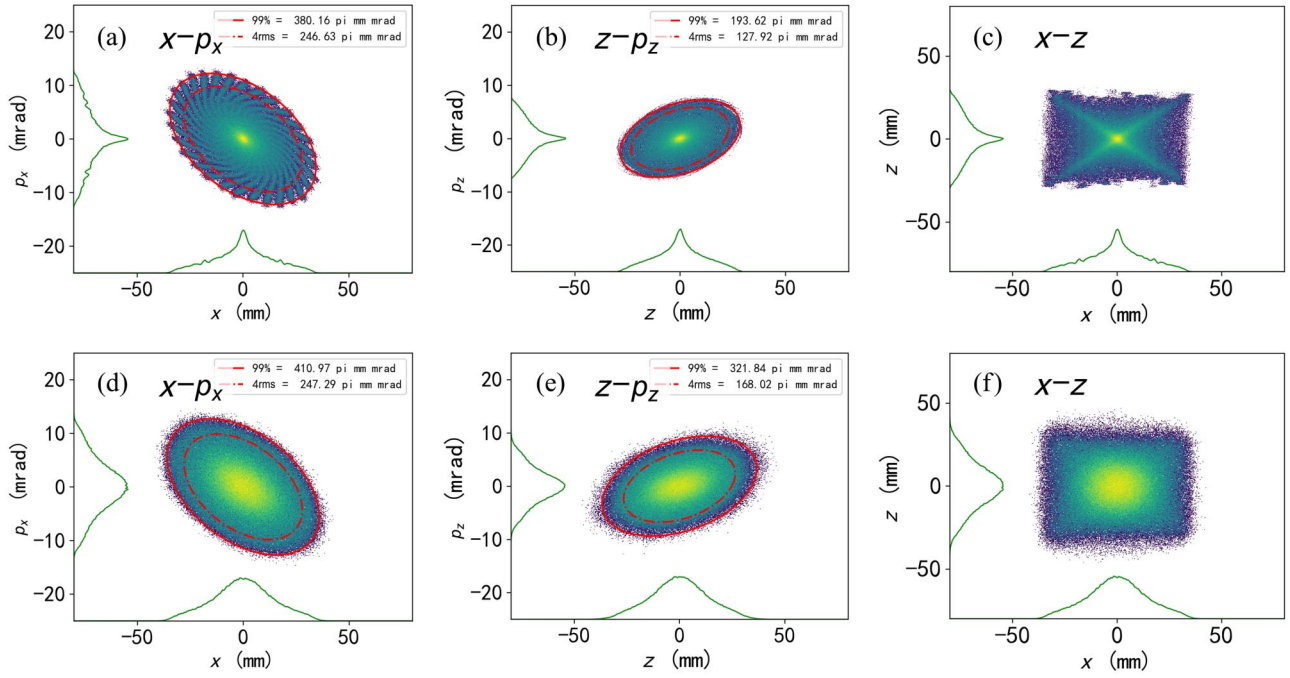



FIG. 11. Phase-space comparison of the accumulated beam without and with space charge. The upper row shows the results without space charge, and the lower row shows the corresponding results including space charge. Panels (a)–(c) show the $x - p_x$, $z - p_z$, and $x - z$ distributions without space charge, respectively. Panels (d)–(f) show the corresponding distributions with space charge.

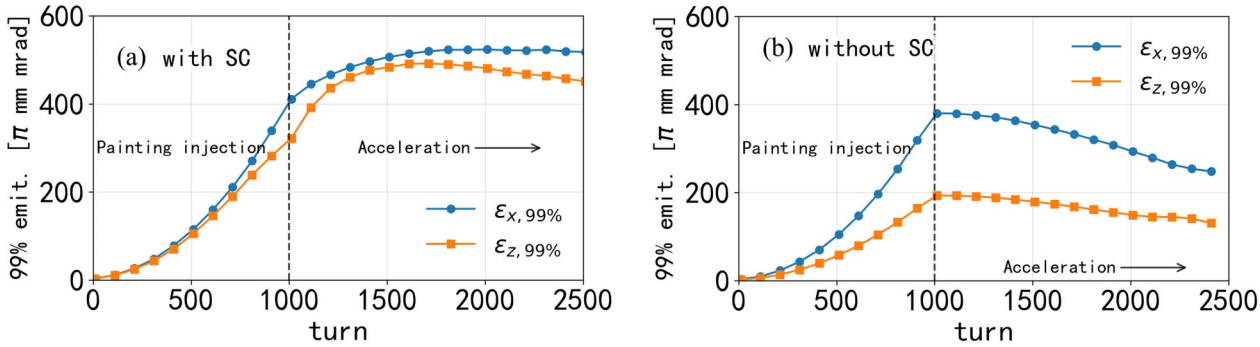



FIG. 12. Evolution of the transverse emittances during beam accumulation. The left and right panels show the results with and without space charge, respectively. The first 1000 turns correspond to the painting injection stage, followed by the acceleration stage.

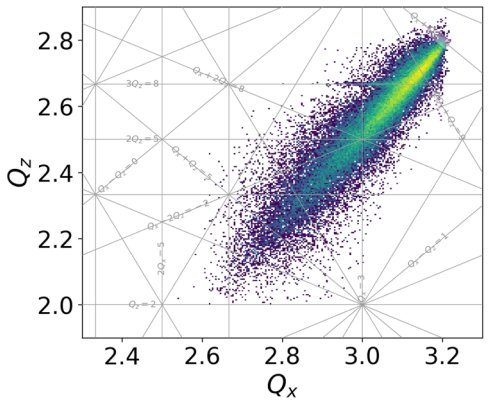



FIG. 13. Space charge tune footprint obtained from the application simulation. The displacement of the footprint from the bare tune represents the space charge tune depression, while its finite width shows that the depression varies with particle amplitude and longitudinal position. The gray lines show nearby resonance conditions.

of emittance growth, and the optimization of painting injection parameters.

## VII. CONCLUSION

Space charge modeling in high-intensity scaling FFAs is challenging for two main reasons. First, the closed orbit changes with energy, so a long bunch cannot be described by a single fixed reference orbit. Second, particle tracking is performed in the global cylindrical coordinate system, which does not directly give the local transverse and longitudinal coordinates and directions needed by a 2.5D space charge solver. These features make conventional 2.5D methods difficult to apply directly.

To address these difficulties, a local 2.5D space charge method has been developed and implemented in the PyFFA code. The method reconstructs the local reference frame from a family of closed orbits at different energies. In this local frame, the bunch can be sliced in the longitudinal direction, the transverse Poisson equation can be solved slice by slice, and the calculated fields can be transformed back to the global tracking coordinates.

The benchmarks collectively validate both the field calculation and the resulting beam dynamics. The transverse and longitudinal fields agree with the corresponding analytical Gaussian solutions. The KV and Gaussian tune-shift benchmarks reproduce the expected linear and amplitude-dependent tune spreads, respectively, with the tune-depression ratios approaching unity as the transverse emittance increases. The rms-envelope comparison further validates the transverse space charge dynamics. The longitudinal dynamics benchmark, through comparison with a reduced 1D analytical model, confirms the implementation of longitudinal space charge.

The method was then applied to a high-intensity scaling FFA case to demonstrate its use in beam accumulation studies, including painting injection, emittance evolution, and tune spread analysis. These examples indicate that the proposed local 2.5D model can provide a practical tool for space charge studies of long, arc-shaped bunches in scaling FFAs.

Future work will extend the present open boundary model to include more realistic vacuum chamber boundary conditions, such as image charge effects [24].

## ACKNOWLEDGMENTS

The authors would like to thank their FFA colleagues for helpful discussions. This work is jointly supported by the Guangdong Basic and Applied Basic Research Foundation (Project No. 2021B1515120021) and Guangdong Special Support Program (Project No. 2024TQ08A570).

## DATA AVAILABILITY

The PyFFA code used in this work is publicly available at Ref. [19]. The simulation data and input files that support the findings of this study are available from the corresponding author upon reasonable request.

## APPENDIX: PARAMETERS OF THE MODELED FFA AND INTENSITY COMPARISON

Figure 14 shows the midplane magnetic lattice together with the injection and extraction closed orbits. Table I summarizes the main lattice, numerical, and beam parameters used in the present study, while Table II compares the modeled intensity with representative operating parameters of existing high-intensity rapid-cycling synchrotrons. Because no directly comparable high-intensity proton FFA is currently in routine operation, CSNS, ISIS, and J-PARC RCS are used as operational references. The facility values correspond to the most recent stable or representative operation found in Refs. [25–27], respectively.

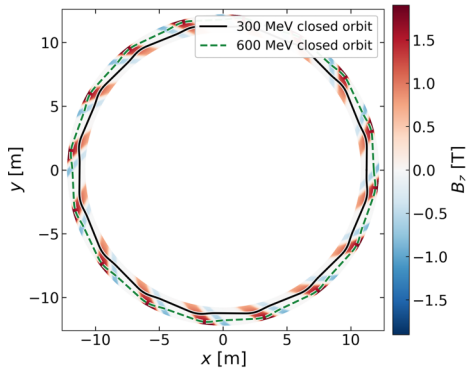



FIG. 14. Layout of the modeled 16-cell FD spiral scaling FFA.

TABLE I. Main lattice, numerical, and beam parameters of the modeled spiral scaling FFA.

| Parameter | Value |
|---|---|
| Lattice type | FD |
| Number of cells | 16 |
| Inj/Ext energy | 300/600 MeV |
| Field index, $k$ | 7.630 |
| Spiral angle | 49.97° |
| Packing factor | 0.394 |
| Reference radius | 12.0 m |
| Reference fields | $+1.650/-0.767$ T |
| F-magnet width | 5.908° |
| D-magnet width | 2.954° |
| F–D drift gap | 2.388° |
| D–F drift gap | 11.250° |
| Fringe-field profile | Sigmoid |
| Bare tunes | $(3.233, 2.813)$ |
| Integration step | 0.02 ns |
| Longitudinal slices | 128 |
| Transverse mesh | $128 \times 128$ |
| Longitudinal rf voltage/turn | 200 kV |
| Repetition rate | 25 Hz |
| Protons per bunch | $2.08 \times 10^{13}$ |
| Beam power | ~50 kW |

TABLE II. Comparison with representative operating parameters of existing high-intensity RCS facilities.

| Parameter | Modeled FFA | CSNS RCS | ISIS RCS | J-PARC RCS |
|---|---|---|---|---|
| Inj/Ext energy (MeV) | 300/600 | 80/1600 | 70/800 | 400/3000 |
| Repetition rate (Hz) | 25 | 25 | 50 | 25 |
| Harmonic number | 1 | 2 | 2 | 2 |
| Protons/pulse ($10^{13}$) | 2.08 | 2.89 | 3.0 | 8.33 |
| Protons/bunch ($10^{13}$) | 2.08 | 1.44 | 1.5 | 4.17 |
| Beam power | 50 kW | 185 kW | 200 kW | 1000 kW |


[1] S. Henderson *et al.*, The spallation neutron source accelerator system design, Nucl. Instrum. Methods Phys. Res., Sect. A **763**, 610 (2014).

[2] H. Takada *et al.*, Materials and life science experimental facility at the Japan proton accelerator research complex i: Pulsed spallation neutron source, Quantum Beam Sci. **1**, 8 (2017).

[3] J. W. G. Thomason, The ISIS spallation neutron and muon source—the first thirty-three years, Nucl. Instrum. Methods Phys. Res., Sect. A **917**, 61 (2019).

[4] H. Chen *et al.*, Design and construction of the China spallation neutron source, Nucl. Instrum. Methods Phys. Res., Sect. A **1078**, 170431 (2025).

[5] R. Garoby *et al.*, The European spallation source design, Phys. Scr. **93**, 014001 (2018).

[6] A. Shishlo, S. Cousineau, J. Holmes, and T. Gorlov, The particle accelerator simulation code PyORBIT, Procedia Comput. Sci. **51**, 1272 (2015).

[7] J. Qiang, Two-and-a-half dimensional symplectic space-charge solver, Phys. Rev. Accel. Beams **28**, 114602 (2025).

[8] S. Machida, Scaling fixed-field alternating-gradient accelerators with reverse bend and spiral edge angle, Phys. Rev. Lett. **119**, 064802 (2017).

[9] S. Machida, R. Barlow, J. S. Berg *et al.*, Acceleration in the linear non-scaling fixed-field alternating-gradient accelerator EMMA, Nat. Phys. **8**, 243 (2012).

[10] S. L. Sheehy, High intensity and other world wide developments in FFAG accelerators, in *Proceedings of the 21st International Conference on Cyclotrons and their Applications (CYCLOTRONS'16)*, Zurich, Switzerland, 2016 (JACoW, Geneva, Switzerland, 2017), pp. 374–379. 10.18429/JACoW-Cyclotrons2016-THD01

[11] T. Uesugi, Y. Ishi, Y. Kuriyama, Y. Mori, C. Jolly, D. J. Kelliher, J.-B. Lagrange, A. P. Letchford, S. Machida, D. W. Posthuma de Boer, C. T. Rogers, E. Yamakawa, and M. Topp-Mugglestone, Beam stacking experiment at a fixed field alternating gradient accelerator, Phys. Rev. Accel. Beams **28**, 012803 (2025).

[12] F. Méot, The ray-tracing code Zgoubi—status, Nucl. Instrum. Methods Phys. Res., Sect. A **767**, 112 (2014).

[13] A. Adelmann, P. Calvo, M. Frey, A. Gsell, U. Locans, C. Metzger-Kraus, N. Neveu, C. Rogers, S. Russell, S. Sheehy, J. Snuverink, and D. Winklehner, OPAL a versatile tool for charged particle accelerator simulations, arXiv:1905.06654.

[14] S. Machida, S-code for fixed field alternating gradient accelerator design and particle tracking, Int. J. Mod. Phys. A **26**, 1794 (2011).

[15] M. Haj Tahar and F. Méot, Space charge in FFAG: A non-linear problem, in *The FFAG 2016 Workshop, Imperial College London* (2016).

[16] M. Haj Tahar, F. Méot, and N. Tsoupas, Space charge studies in FFAG using the tracking code ZGOUBI, in *Proceedings of IPAC2015, Richmond, VA, USA* (JACoW, Geneva, Switzerland, 2015), pp. 717–719.

[17] J. J. Yang, A. Adelmann, M. Humbel, M. Seidel, and T. J. Zhang, Beam dynamics in high intensity cyclotrons including neighboring bunch effects: Model, implementation, and application, Phys. Rev. ST Accel. Beams **13**, 064201 (2010).

[18] S. Machida, Space charge issues in FFAs, lecture slides, International FFA School, 2025.

[19] K. Zhou, PyFFA: Python toolkit for high-intensity FFA beam dynamics simulation, https://github.com/acphymeow/PyFFA (2025).

[20] T. L. Hart, D. J. Summers, and K. Paul, Magnetic field expansion out of a plane: Application to cyclotron development, in *Proceedings of the 2011 Particle Accelerator Conference (PAC'11)* (PAC'11 Organizing Committee/IEEE, New York, NY, USA, 2011), pp. 1846–1848.

[21] Y. Shobuda, Calculation of space-charge tune shift in a cylindrical chamber for bunched beams employing Green's function formalism, Phys. Rev. Accel. Beams **27**, 011001 (2024).

[22] Y.-S. Yuan, Modeling of beam envelope instabilities in high-intensity circular accelerators, Phys. Rev. Res. **7**, 043239 (2025).

[23] S. Y. Lee, G. Franchetti, I. Hofmann, F. Wang, and L. Yang, Emittance growth mechanisms for space-charge dominated beams in fixed field alternating gradient and proton driver rings, New J. Phys. **8**, 291 (2006).

[24] M. Migliorati, N. Biancacci, M. R. Masullo, L. Palumbo, and V. G. Vaccaro, Space charge impedance and electromagnetic fields in elliptical vacuum chambers, Phys. Rev. Accel. Beams **21**, 124201 (2018).

[25] Institute of High Energy Physics, Chinese Academy of Sciences, Milestone reached for china's large-scale scientific facility as CSNS runs at 185 kw, https://english.ihep.cas.cn/nw/han/y26/202603/t20260317_1152755.html (2026).

[26] R. E. Williamson, D. J. Adams, H. V. Cavanagh, B. Kyle, D. W. Posthuma de Boer, H. Rafique, and C. M. Warsop, High-intensity studies on the ISIS RCS and their impact on the design of ISIS-II, in *Proceedings of the 68th ICFA Advanced Beam Dynamics Workshop on High-Intensity and High-Brightness Hadron Beams (HB2023)* (JACoW Publishing, Geneva, Switzerland, 2023), pp. 331–337. 10.18429/JACoW-HB2023-THA1I2.

[27] P. K. Saha, H. Harada, Y. Shobuda, F. Tamura, K. Kojima, M. Yoshimoto, H. Okita, K. Okabe, I. Yamada, M. Chimura, K. Moriya, T. Takayanagi, M. Yamamoto, and K. Yamamoto, Beyond 1 MW operation of the J-PARC RCS, in *Proceedings of the 16th International Particle Accelerator Conference (IPAC2025)* (JACoW Publishing, Geneva, Switzerland, 2025), pp. 936–939. 10.18429/JACoW-IPAC2025-TUPB003.